PHYSICAL REVIEW A **69**, 022703 (2004)

Complete direct method for electron-hydrogen scattering: Application to the collinear and Temkin-Poet models

Philip L. Bartlett* and Andris T. Stelbovics†
Centre for Atomic, Molecular and Surface Physics, Murdoch University, Perth 6150, Australia

(Received 5 September 2003; published 4 February 2004)

We present an efficient generalization of the exterior complex scaling (ECS) method to extract discrete inelastic and ionization amplitudes for electron-impact scattering of atomic hydrogen. This fully quantal method is demonstrated over a range of energies for the collinear and Temkin-Poet models and near-threshold ionization is examined in detail for singlet and triplet scattering. Our numerical calculations for total ionization cross sections near threshold strongly support the classical threshold law of Wannier [Phys. Rev. **90**, 817 (1953)] ($\sigma \propto E^{1.128\pm0.004}$) for the $L=0$ singlet collinear model and the semiclassical threshold law of Peterkop [J. Phys. B **16**, L587 (1983)] ($\sigma \propto E^{3.37\pm0.02}$) for the $L=0$ triplet collinear model, and are consistent with the semiclassical threshold law of Macek and Ihra [Phys. Rev. A **55**, 2024 (1997)] ($\sigma \propto \exp[(-6.87\pm0.01)E^{-1/6}]$) for the singlet Temkin-Poet model.

DOI: 10.1103/PhysRevA.69.022703 PACS number(s): 34.80.Dp, 34.10.+x

I. INTRODUCTION

In a recent publication Baertschy *et al.* [1] demonstrated that the method of exterior complex scaling (ECS) could be successfully applied to the Coulomb three-body problem of electron-impact ionization. This was a significant breakthrough in the field of electron collisions as they showed that the time independent Schrödinger equation could be used to calculate the scattered wave function without explicit knowledge of the asymptotic boundary conditions, which until recently [2] were not known for the full electron-hydrogen problem. Clearly, the ability to solve many-body problems, particularly above ionization threshold, without knowledge of their boundary conditions makes the ECS method invaluable for larger more complex systems. However, implementation of the ECS method of Baertschy *et al.* involves solving very large and sparse systems of linear equations, making its application to a four-body problem (for example, the electron-impact double ionization of helium) impractical with current supercomputing technology.

In an effort to reduce the computational overhead of the direct solution of the electron-hydrogen problem using ECS, as an incremental step towards solving the four-body problem, we have adopted a propagation technique, originally used by Poet [3] to solve the Temkin-Poet [4,5] (TP) model problem. More recently it was used by Jones and Stelbovics [6,7] for benchmark calculations for the TP ionization model. In this paper we generalize this propagation method so that it can be used with ECS. We believe that this algorithm has features that will lead to a significant saving in the computational requirement of the full hydrogen problem.

Once the scattering wave function has been computed there still remains the problem of extracting the scattering amplitudes. The application of the ECS method has focused thus far primarily on the ionization amplitude (e.g., Refs. [8–12]). We show how the integral formulation for extracting ionization amplitudes can be adopted to compute any discrete excitation amplitude. We give numerous examples for the collinear [13,14] (CL) and TP models.

The work of Baertschy *et al.* [1] for the ECS solution to the full hydrogen problem was preceded by many publications which explored the theoretical basis for ECS [15], application of ECS to short-range potential models [10], and benchmark calculations for the TP model [8,9]. Later publications explored integral methods for extracting ionization amplitudes for the CL and TP models [11] as well as the full hydrogen problem [12], in contrast to their previous flux extrapolation method. Our work is also based on this integral method for extracting ionization cross sections, originally proposed by Peterkop [16] and Rudge and Seaton [17].

For the CL model, the efficiency of the present method has allowed us to probe significantly lower energies, which requires much larger grids, with greater accuracy than previous fully quantal studies [11,18,19]. This allowed us to investigate the classical Wannier [20] threshold law for the $L=0$ singlet CL model, and provide a fitting function that accurately predicts the low-energy behavior of its total ionization cross section (TICS) [21]. Similar procedures were used to calculate the fully quantal threshold power law for the $L=0$ triplet CL model, which supports the semiclassical calculations of Peterkop [22], and the threshold behavior of the singlet TP model, which is consistent with the calculations of Macek and Ihra [23].

We have also explored the phase of the ionization amplitude extracted from the ECS wave functions for several different configurations of the final-state continuum waves. We were able to calculate cross sections using several choices for these continuum waves, and found, as detailed in previous ECS publications by McCurdy *et al.* [11] for the model problems and Baertschy *et al.* [12] for the full hydrogen problem, that the product of two Coulomb waves, with equal charge, provides an accurate and smooth single-differential cross sections (SDCS). However, for the TP model we have demonstrated that convergence of the ionization amplitude phase is only achieved directly when this final state is repre-

---

*Electronic address: bartlett@fizzy.murdoch.edu.au
†Electronic address: stelbovi@fizzy.murdoch.edu.au

sented by a plane wave for the fast electron and a Coulomb wave for the slow electron [24], which represents the true asymptotic boundary conditions for this model. In the CL model, neither of these choices for the final-state continuum wave provides convergent phases. However, a recent paper by Rescigno *et al.* [25] gives correction formulas for the ionization amplitude phases for both the CL and TP models when the final-state continuum waves are approximated by two Coulomb waves of arbitrary charges. We test these formulas for these models for both the singlet and triplet wave functions.

II. THEORY

A. Scattered wave equations

The Schrödinger equation for the electron-impact of hydrogen is $\hat{H}\Psi^{(+)}=E\Psi^{(+)}$, and using the relationship $\Psi^{(+)}=\Psi^{\mathrm{sc}(+)}+\Psi_{\boldsymbol{k}_i}$ may also be expressed as

$$(E-\hat{H})\Psi^{\mathrm{sc}(+)}(\boldsymbol{r}_1,\boldsymbol{r}_2)=(\hat{H}-E)\Psi_{\boldsymbol{k}_i}(\boldsymbol{r}_1,\boldsymbol{r}_2), \tag{1}$$

where $\Psi^{\mathrm{sc}(+)}$ is the scattered outgoing wave function and $\Psi_{\boldsymbol{k}_i}$ is the symmetrized initial-state wave function given by

$$\Psi_{\boldsymbol{k}_i}(\boldsymbol{r}_1,\boldsymbol{r}_2)=\frac{1}{\sqrt{2}}[\Phi_{1s}(\boldsymbol{r}_1)e^{i\boldsymbol{k}_i\cdot\boldsymbol{r}_2}+(-1)^S(1\leftrightarrow 2)]. \tag{2}$$

Φ_{1s} is the hydrogen ground-state wave function, $\boldsymbol{k}_i$ is the momentum of the incident-electron, and the Hamiltonian of the system is given by

$$\hat{H}=-\frac{1}{2}\nabla_1^2-\frac{1}{2}\nabla_2^2-\frac{1}{r_1}-\frac{1}{r_2}+V_{12}(\boldsymbol{r}_1,\boldsymbol{r}_2), \tag{3}$$

where for the full hydrogen problem

$$V_{12}(\boldsymbol{r}_1,\boldsymbol{r}_2)=\frac{1}{|\boldsymbol{r}_1-\boldsymbol{r}_2|}. \tag{4}$$

All equations, unless otherwise noted, are in atomic units (a.u.).

The CL and TP models calculated in this paper are simplifications of the full hydrogen problem, and we only consider the case where all angular momenta are zero, and the hydrogen target is initially in the ground state [26]. After performing a partial-wave expansion of Eq. (1) using

$$\Psi^{\mathrm{sc}(+)}(\boldsymbol{r}_1,\boldsymbol{r}_2)=\frac{1}{r_1 r_2}\sum_{l_1 l_2 L}\psi^L_{l_1 l_2}(r_1,r_2)\mathcal{Y}^{L0}_{l_1 l_2}(\hat{\boldsymbol{r}}_1,\hat{\boldsymbol{r}}_2) \tag{5}$$

and retaining only zero angular momentum terms we have

$$\left(E+\frac{1}{2}\frac{\partial^2}{\partial r_1^2}+\frac{1}{2}\frac{\partial^2}{\partial r_2^2}+\frac{1}{r_1}+\frac{1}{r_2}-V_{12}(r_1,r_2)\right)\psi(r_1,r_2)=\chi(r_1,r_2), \tag{6}$$

where $\psi=\psi^L_{l_1 l_2}$ is the outgoing scattered wave function for $L=l_1=l_2=0$, and

$$\chi(r_1,r_2)=\frac{\sqrt{2\pi}}{k_i}\left[\left(V_{12}(r_1,r_2)-\frac{1}{r_2}\right)\phi_{1s}(r_1)\sin(k_i r_2)+(-1)^S(1\leftrightarrow 2)\right], \tag{7}$$

where $\phi_{1s}(r)=rR_{1s}(r)$ and $R_{1s}(r)$ is the radial wave function for the ground state $(n=1,l=0)$ of hydrogen.

For the TP model the V_{12} term, derived from the first term of the partial-wave expansion of the electron-electron potential $(1/|\boldsymbol{r}_1-\boldsymbol{r}_2|)$, is given by

$$V_{12}(r_1,r_2)=\frac{1}{r_>}=\frac{1}{\max(r_1,r_2)}. \tag{8}$$

The CL model is a low-energy approximation of the full problem, and can be viewed as one where the ejected and scattered electrons leave the nucleus in opposite directions, giving an electron-electron potential of

$$V_{12}(r_1,r_2)=\frac{1}{r_1+r_2}. \tag{9}$$

B. Exterior complex scaling

We solved Eq. (6) using the method of exterior complex scaling, where all radial coordinates are rotated into the complex plane by a fixed angle θ, at a sufficiently large radius R_0, such that convergence of the extracted cross sections is obtained. This transformation,

$$z(r)=\begin{cases} r, & r<R_0\\ R_0+(r-R_0)e^{i\theta}, & r\geqslant R_0,\end{cases} \tag{10}$$

allows a numerical solution to be calculated without knowledge of the asymptotic boundary conditions, as all outgoing waves diminish exponentially beyond R_0. The scattered wave function contains only outgoing waves, but the inhomogeneous term χ contains both incoming and outgoing waves, and so must be truncated at R_0, as incoming waves diverge using this transformation. This method has been used successfully by McCurdy *et al.* [11] for the models considered in this paper, and later by Baertschy *et al.* [1] for the full hydrogen problem.

Rescigno *et al.* [15] demonstrated that finite difference methods may be used to solve this ECS transformation, provided that R_0 is one of the grid points. The application of this transformation to the numerical solution of Eq. (6) is equivalent to solving the finite-difference equations for Eq. (6) without transformation, but using complex grid spacing beyond R_0.

C. Discrete final-state cross sections

The method we use to compute the discrete final-state scattering amplitudes is based on the integral [27]

$$I=\int \Psi^{(+)}(\boldsymbol{r}_1,\boldsymbol{r}_2)(\hat{H}-E)\Phi^*(\boldsymbol{r}_1,\boldsymbol{r}_2)d\boldsymbol{r}_1 d\boldsymbol{r}_2, \tag{11}$$

where Φ is an asymptotic approximation of the final state. The energy and potential operators can be removed by using the relationship $(\hat{H}-E)\Psi^{(+)}(\boldsymbol{r}_1,\boldsymbol{r}_2)=0$, giving

$$I=\frac{1}{2}\int \{\Phi^*(\boldsymbol{r}_1,\boldsymbol{r}_2)(\nabla_1^2+\nabla_2^2)\Psi^{(+)}(\boldsymbol{r}_1,\boldsymbol{r}_2) -\Psi^{(+)}(\boldsymbol{r}_1,\boldsymbol{r}_2)(\nabla_1^2+\nabla_2^2)\Phi^*(\boldsymbol{r}_1,\boldsymbol{r}_2)d\boldsymbol{r}_1 d\boldsymbol{r}_2\}. \tag{12}$$

By rearrangement, and use of the divergence theorem, this may then be converted into a surface integral over one coordinate and a volume integral over the other coordinate

$$I=\int d^3r_2 \oint_{S_1}[\Phi^*(\boldsymbol{r}_1,\boldsymbol{r}_2)\nabla_1\Psi^{(+)}(\boldsymbol{r}_1,\boldsymbol{r}_2) -\Psi^{(+)}(\boldsymbol{r}_1,\boldsymbol{r}_2)\nabla_1\Phi^*(\boldsymbol{r}_1,\boldsymbol{r}_2)]\cdot d\boldsymbol{S}_1, \tag{13}$$

where we have also made use of the antisymmetry of $\Psi^{(+)}$ and Φ in writing this form.

To derive the relationship between I and the scattering amplitude f_{ji}, where the subscripts $i\equiv(n_i l_i m_i)$ and $j\equiv(n_j l_j m_j)$ are the initial and final state of the target hydrogen atom, we substitute into Eq. (13) an asymptotic approximation for the outgoing scattering wave function given by

$$\Psi_i^{\mathrm{sc}(+)}(\boldsymbol{r}_1,\boldsymbol{r}_2)\sim\frac{1}{\sqrt{2}}\sum_j \Phi_j(\boldsymbol{r}_2)\frac{e^{+ik_j r_1}}{r_1}f_{ji}(\boldsymbol{k}_j,\boldsymbol{k}_i), \tag{14}$$

when $r_1\rightarrow\infty$, $r_2/r_1\rightarrow 0$, and an asymptotic approximation of the final state given by

$$\Phi_j(\boldsymbol{r}_1,\boldsymbol{r}_2)=\frac{1}{\sqrt{2}}[\Phi_j(\boldsymbol{r}_1)e^{i\boldsymbol{k}_j\cdot\boldsymbol{r}_2}+(-1)^S(1\leftrightarrow 2)]. \tag{15}$$

We can use the outgoing scattering wave function $\Psi_i^{\mathrm{sc}(+)}$ in place of the outgoing total wave function $\Psi^{(+)}$ in Eq. (13), as asymptotically the initial-state wave function does not contribute to the integral. Then, by substituting the asymptotic form for a plane wave (in three dimensions),

$$e^{i\boldsymbol{k}\cdot\boldsymbol{r}}\sim\frac{2\pi}{ikr}[\delta(\hat{\Omega}_{\boldsymbol{k}}-\hat{\Omega}_{\boldsymbol{r}})e^{ikr}-\delta(\hat{\Omega}_{\boldsymbol{k}}+\hat{\Omega}_{\boldsymbol{r}})e^{-ikr}], \tag{16}$$

and removing terms that asymptotically approach zero, we arrive at the relationship

$$f_{ji}(\boldsymbol{k}_j,\boldsymbol{k}_i)=\frac{(-1)^{S+1}}{2\pi}I, \tag{17}$$

and can calculate the scattering cross section using

$$\sigma_{ji}=\frac{k_j}{k_i}\int |f_{ji}(\boldsymbol{k}_j,\boldsymbol{k}_i)|^2 d\hat{\boldsymbol{k}}_j, \tag{18}$$

where $\boldsymbol{k}_j$ is the momentum of the scattered electron. The magnitude of this momentum, for a ground state target, is given by $k_j=k_i-\frac{1}{2}(1-1/n_j^2)$. For the $L=0$ models considered in this paper, this simplifies to

$$\sigma_{ji}=4\pi\frac{k_j}{k_i}|f_{ji}(k_j)|^2. \tag{19}$$

To evaluate f_{ji} for the $L=0$ models considered here, we perform a partial-wave expansion by substituting

$$\Psi_i^{\mathrm{sc}(+)}(\boldsymbol{r}_1,\boldsymbol{r}_2)=\frac{1}{r_1 r_2}\sum_{\substack{l_1 l_2\\ LM\Pi}} i^L \psi_{l_1 l_2}^{SLM\Pi}(r_1,r_2)\mathcal{Y}_{l_1 l_2}^{LM}(\widehat{\boldsymbol{r}_1},\widehat{\boldsymbol{r}_2}), \tag{20}$$

$$\Phi_j(\boldsymbol{r}_1,\boldsymbol{r}_2)=\frac{1}{\sqrt{2}}\left(\frac{1}{r_1}\phi_{n_j l_j}(r_1)Y_{l_j m_j}(\hat{\boldsymbol{r}}_1)e^{i\boldsymbol{k}_j\cdot\boldsymbol{r}_2} +(-1)^S(1\leftrightarrow 2)\right), \tag{21}$$

and

$$e^{i\boldsymbol{k}\cdot\boldsymbol{r}}=4\pi\sum_{l=0}^{\infty}\sum_{m=-l}^{l} i^l j_l(kr)Y_{lm}^*(\hat{\boldsymbol{k}})Y_{lm}(\hat{\boldsymbol{r}}) \tag{22}$$

into Eq. (13) and Eq. (17). By retaining only the $L=l_1=l_2=0$ terms, and using the notation $\psi(r_1,r_2)=\psi_{00}^{S000}(r_1,r_2)$, we were able to derive the asymptotic form for the discrete final-state scattering amplitude for the $L=l_1=l_2=0$ case as

$$f_{ji}(k_j)\sim\frac{1}{\sqrt{2\pi}}\int dr_2 r_1^2\phi_{n_j 0}(r_2)\left[\frac{1}{r_1}\psi(r_1,r_2)\frac{\partial}{\partial r_1}j_0(k_j r_1)-j_0(k_j r_1)\frac{\partial}{\partial r_1}\frac{1}{r_1}\psi(r_1,r_2)\right], \tag{23}$$

where j_0 is the spherical Bessel function for $l=0$.

D. Ionization cross sections

The TICS results were extracted from the scattered wave function using the equation for ionization amplitude given in Eq. (11). Details of the method leading to the limiting expressions on a hypersphere have been given previously by McCurdy and Rescigno [10] and will not be repeated here. For our $L=0$ model problems the TICS is given by

$$\sigma(E)=\int_0^{E/2}\frac{16}{\pi k_i k_1 k_2}|f(k_1,k_2,R)|^2 d\epsilon_2, \tag{24}$$

where

$$f(k_1,k_2,R)\sim\frac{R}{2}\int_0^{\pi/2}d\alpha\left[\Phi^*(k_1,k_2,R,\alpha)\frac{\partial}{\partial R}\psi(R,\alpha)\right.$$
$$\left.-\psi(R,\alpha)\frac{\partial}{\partial R}\Phi^*(k_1,k_2,R,\alpha)\right], \tag{25}$$

where the total system energy is given by $E=\epsilon_1+\epsilon_2=(k_1^2+k_2^2)/2$, the hyperangle is given by $\alpha=\arctan(r_2/r_1)$, and the hyperradius is given by $R=\sqrt{r_1^2+r_2^2}$. Φ is a function that describes the final-state asymptotic continuum waves of the ionization process.

This method for extracting the TICS from the scattered wave function has been used successfully by McCurdy *et al.* [11] for the model hydrogen problems considered in this paper, and by Baertschy *et al.* [12] for the full problem. In both of these papers the final-state continuum waves are approximated by the product of two Coulomb waves with charge $z=1$.

$$\Phi(k_1,r_1,k_2,r_2)=\phi_{l_1}^{(-)}(k_1,r_1)\phi_{l_2}^{(-)}(k_2,r_2), \tag{26}$$

where $l_1=l_2=0$ for the model problems considered in this paper.

However, it is known that for the TP model this choice of continuum waves leads to a divergent ionization amplitude phase [24,25]. As it is also known that the boundary condition of the TP model is a plane wave and Coulomb wave, which has the form

$$\Phi^{(-)}(k_1,r_1,k_2,r_2)=\phi_{l_1}^{(-)}(k_1r_1)\sin(k_2r_2),\quad k_1<k_2, \tag{27}$$

we also present SDCS calculations for this choice of continuum waves. However, to ensure that the discrete excitation states of hydrogen, which are also contained in ψ, do not affect the ionization amplitude, we have made the $\langle r|k\rangle=\sin(kr)$ function orthogonal to the first N bound states of hydrogen (with $l=0$) using the relation

$$\langle r|k\rangle_\perp=\langle r|k\rangle-\sum_n^N\langle r|n00\rangle\langle n00|k\rangle, \tag{28}$$

where N can be made arbitrarily large. As $\langle r|k\rangle_\perp=\langle r|k\rangle$ for $r\rightarrow\infty$, the orthogonalization of the plane wave has no effect upon the asymptotic value of Eq. (25). However, for the finite values of R used in our numerical calculations, the orthogonalization of the plane wave removes interference from discrete final-state scattering amplitudes.

Previously, it was shown by McCurdy and Rescigno [10] that for a short-range potential problem, using a projection operator to project out the elastic channel from the scattering wave function removes the wildly oscillatory behavior due to the discrete channels of the problem. Our orthogonalization of the plane wave is equivalent to their procedure.

III. COMPUTATIONAL METHODS

A. Numerov formula

The Numerov formula was used to numerically solve Eq. (6) on a two-dimensional grid of points (symmetric in r_1 and r_2). When translated to two dimensions the Numerov formula uses grid point values of $\psi(i,j)$ and its eight nearest neighbors. The derivation of this formula was given by Poet [3], and allowed for the singularity at $r_1=0$ and $r_2=0$ by using a series expansion of ψ at these points. However, a further modification to the Numerov formula was required to allow for the transition from real to complex coordinates at R_0. A benefit of our modified Numerov formula presented in the Appendix is that it allows for arbitrary grid spacing in other regions (both real and complex), removing the restriction of most Numerov implementations of either constant grid spacing (e.g., Refs. [28,29]) or grid-doubling methods (e.g., Ref. [7]).

McCurdy *et al.* [11] observed small oscillations in their extracted cross sections, which diminish with increasing R_0, and attributed them to diffraction effects caused by using finite grid methods. These oscillations were reduced by smoothly truncating the V_{12} potential on the left-hand side of Eq. (6) near R_0 using

$$\tilde{V}_{12}(r_1,r_2)=V_{12}(r_1,r_2)\exp(-(R/R_0)^{(R_0/3)}), \tag{29}$$

where R is the hyperradius. These effects were only noticeable in our calculations at low incident energies, or small R_0, however, we have applied the same smooth truncation when calculating *all* the results presented in this paper.

B. Propagation method

To minimize the computational overhead we used a propagation method similar to that of Poet [3], and recently used by Jones and Stelbovics [29] for the TP model, but was modified to allow for the inhomogeneous term χ in this problem. The notation we use for the $\boldsymbol{A}$, $\boldsymbol{B}$, $\boldsymbol{C}$, and $\boldsymbol{D}$ matrices is defined in Ref. [29], and should be referred to, in conjunction with Ref. [3], to obtain a detailed understanding of the grid labeling, etc. The Numerov formula for Eq. (6) may be represented in matrix form as

$$\boldsymbol{A}^{(i)}\cdot\vec{\boldsymbol{\psi}}^{(i-1)}+\boldsymbol{B}^{(i)}\cdot\vec{\boldsymbol{\psi}}^{(i)}+\boldsymbol{C}^{(i)}\cdot\vec{\boldsymbol{\psi}}^{(i+1)}=\vec{\boldsymbol{\chi}}^{(i)}, \tag{30}$$

where the ith column of the grid is solved at each step. This equation can be reformed into the propagation equation

$$\vec{\boldsymbol{\psi}}^{(i)}=\boldsymbol{D}^{(i)}\cdot\vec{\boldsymbol{\psi}}^{(i+1)}+\boldsymbol{E}^{(i)}, \tag{31}$$

where the $\vec{\boldsymbol{E}}$ propagation vector has been introduced into our derivation, to allow for the inhomogeneous term. The propagation matrix and propagation vector are then given by

$$\boldsymbol{D}^{(i)} = -\tilde{\boldsymbol{B}}^{(i)} \cdot \boldsymbol{C}^{(i)}, \tag{32}$$

$$\tilde{\boldsymbol{B}}^{(i)} = (\boldsymbol{B}^{(i)} + \boldsymbol{A}^{(i)} \cdot \boldsymbol{D}^{(i-1)})^{-1}, \tag{33}$$

$$\vec{\boldsymbol{E}}^{(i)} = \tilde{\boldsymbol{B}}^{(i)} \cdot (\vec{\boldsymbol{\chi}}^{(i)} - \boldsymbol{A}^{(i)} \cdot \vec{\boldsymbol{E}}^{(i-1)}), \tag{34}$$

noting that $i \geqslant 1$ and the boundary conditions are $\vec{\boldsymbol{\psi}}^{(0)} = \vec{\boldsymbol{0}}$ and $\vec{\boldsymbol{\psi}}^{(i)}(0) = 0$.

The symmetry of the scattered wave function is given by $\psi(r_1,r_2) = (-1)^S \psi(r_2,r_1)$, and so Eq. (6) need only be solved in the lower triangular region bounded by $r_2 = 0$, $r_1 = r_2$, and $r_1 = R_{max} > R_0$, hence the size of the propagation matrices increase with increasing i. It should be noted that the matrices have the following dimensions: $\boldsymbol{A}^{(i)}(i,i-1)$, $\boldsymbol{B}^{(i)}(i,i)$, $\tilde{\boldsymbol{B}}^{(i)}(i,i)$, $\boldsymbol{C}^{(i)}(i,i+1)$, and $\boldsymbol{D}^{(i)}(i,i+1)$, where $\boldsymbol{A}^{(i)}$, $\boldsymbol{B}^{(i)}$, and $\boldsymbol{C}^{(i)}$ are band matrices and $\tilde{\boldsymbol{B}}^{(i)}$ and $\boldsymbol{D}^{(i)}$ are dense matrices, and are real for $i < i_{R_0}$ and complex for $i \geqslant i_{R_0}$. The vast majority of the computational effort is devoted to the matrix inversion in Eq. (33).

Detailed descriptions of this method may be obtained from other authors including Poet [3], Jones and Stelbovics [6], and Wang and Callaway [28], and will not be repeated in this paper. Where our procedure differs from these previous studies, is that due to the ECS transformation an asymptotic approximation of the solution is not required at the edges of our grid ($r_1 = R_{max}$ and $r_2 = R_{max}$), as the transformed wave function can be set to zero on these boundaries.

In order to evaluate the scattering wave function over the entire grid, the $\boldsymbol{A}^{(i)}$, $\tilde{\boldsymbol{B}}^{(i)}$, and $\boldsymbol{C}^{(i)}$ matrices must be retained for all i. For most of the calculations presented in this paper, the memory required for this storage greatly exceeded the memory capacity of the single supercomputer node that we used for each calculation (4 gigabytes). Moreover, for several of the calculations with very large R_{max}, the storage requirement even exceeded the available high bandwidth hard disk capacity of the node (50 gigabytes), so we implemented a method of writing the $\tilde{\boldsymbol{B}}^{(i)}$ matrices to disk only at certain milestone values of i, during the forward pass of the propagation algorithm [evaluating Eqs. (32)–(34)].

On the backward pass [evaluating Eq. (31)], the $\tilde{\boldsymbol{B}}^{(i)}$ matrices between the milestone values of i were required to be recalculated. This resulted in an overall doubling of computation time, but allowed us to extend to very large grids without being limited by memory or hard disk capacity.

C. Integration and interpolation

It should be noted that the integrand in Eq. (25) is *highly* oscillatory, and to ensure accurate calculation suitable integration techniques must be employed. For example, the ionization amplitude integral for the TP model at equal energy sharing, $E_0 = 2$ a.u. and $R_0 = 400$ a.u., were of the order of 150 oscillations. We used an adaptive grid-halving method based upon the 10-point Bode's rule [30] to evaluate this integral, which required the order of 2000 points for an estimated 0.001% accuracy. Also, it is important that the interpolation routine used to calculate values for $\psi(r_1,r_2)$, between grid points is very accurate. We used Chebyshev polynomials fitted to a 10×10 grid containing the selected point. We also noted that when using finite-difference methods to calculate the $\partial\psi/\partial R$ terms, all the points required to calculate the derivative should be calculated using the same 10×10 grid (even when some of the points cross into a different grid square), otherwise slight discontinuities appeared in the integrand, which caused problems for our adaptive integration routine.

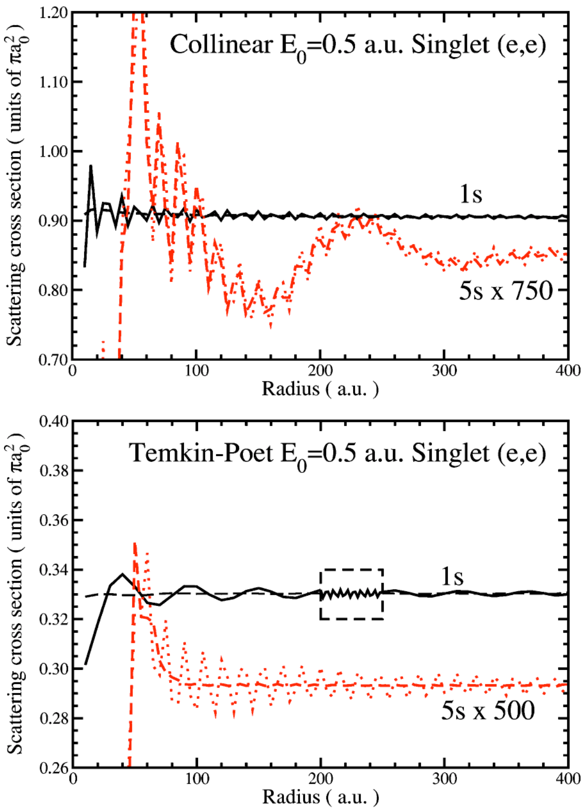

FIG. 1. CL and TP singlet (e,e) $1s$ and $5s$ final-state scattering cross sections at ionization threshold (0.5 a.u.), with spin weighting, as a function of the hypercube dimension used in Eq. (23). The solid and dotted lines are the raw results, and the long dashes are the results after scaling by $[1+n\,\sin(2k_nR)/R]$.

IV. RESULTS

A. Discrete final-state cross sections

Using Eqs. (19) and (23) we were able to successfully extract the discrete final-state cross sections from our scattering wave functions for both the CL and TP models. However, as is evident from Fig. 1, the cross sections exhibit a slowly diminishing oscillatory behavior with respect to R (approximately $1/R$). The relative amplitude of these oscillations increase (approximately linearly) with the final n state of the hydrogen target, and their wavelength also increases (approximately linearly) with n. These oscillations increase

TABLE I. CL model singlet (σ^0) and triplet (σ^1) electron-impact discrete final-state scattering cross sections σ_{ns} and total ionization cross sections σ_i, where n is the final orbital quantum number of the target hydrogen atom, σ_t is the total electron-impact cross section, E_0 is the incident-electron energy (a.u.), and cross section units are πa_0^2. Numbers in square brackets indicate powers of 10.

E_0	σ^0_{1s}	σ^0_{2s}	σ^0_{3s}	σ^0_{4s}	σ^0_{5s}	σ^0_i	σ^0_t	σ^1_{1s}	σ^1_{2s}	σ^1_{3s}	σ^1_{4s}	σ^1_{5s}	σ^1_i	σ^1_t
0.1	1.11[+0]						1.11[+0]	1.60[−3]						1.60[−3]
0.2	1.63[+0]						1.63[+0]	1.86[+0]						1.86[+0]
0.3	1.39[+0]						1.39[+0]	2.63[+0]						2.63[+0]
0.4	1.09[+0]	3.71[−2]					1.13[+0]	2.69[+0]	9.79[−4]					2.69[+0]
0.5	9.05[−1]	2.31[−2]	5.97[−3]	2.36[−3]	1.13[−3]		9.38[−1]	2.51[+0]	2.82[−3]	1.17[−4]	1.26[−5]	2.24[−6]		2.51[+0]
0.6	7.62[−1]	1.68[−2]	4.46[−3]	1.81[−3]	9.21[−4]	6.01[−3]	7.92[−1]	2.27[+0]	4.09[−3]	3.85[−4]	9.34[−5]	3.55[−5]	4.06[−5]	2.27[+0]
0.7	6.56[−1]	1.27[−2]	3.39[−3]	1.38[−3]	7.04[−4]	9.03[−3]	6.83[−1]	2.05[+0]	4.81[−3]	6.13[−4]	1.80[−4]	7.73[−5]	2.35[−4]	2.06[+0]
0.8	5.72[−1]	9.99[−3]	2.63[−3]	1.08[−3]	5.43[−4]	1.02[−2]	5.96[−1]	1.83[+0]	5.11[−3]	7.61[−4]	2.45[−4]	1.09[−4]	5.48[−4]	1.84[+0]
0.9	5.05[−1]	8.05[−3]	2.10[−3]	8.58[−4]	4.30[−4]	1.04[−2]	5.27[−1]	1.65[+0]	5.18[−3]	8.49[−4]	2.87[−4]	1.31[−4]	9.06[−4]	1.66[+0]
1.0	4.50[−1]	6.64[−3]	1.71[−3]	6.96[−4]	3.52[−4]	1.01[−2]	4.69[−1]	1.48[+0]	5.11[−3]	8.90[−4]	3.09[−4]	1.45[−4]	1.26[−3]	1.49[+0]
1.5	2.82[−1]	3.19[−3]	7.91[−4]	3.15[−4]	1.60[−4]	7.26[−3]	2.94[−1]	9.40[−1]	4.09[−3]	8.21[−4]	3.01[−4]	1.47[−4]	2.39[−3]	9.48[−1]
2.0	1.98[−1]	1.91[−3]	4.63[−4]	1.83[−4]	9.22[−5]	5.04[−3]	2.06[−1]	6.52[−1]	3.12[−3]	6.58[−4]	2.47[−4]	1.21[−4]	2.68[−3]	6.59[−1]

with decreasing electron-impact energy, and as they remain constant when finer grid spacing is used, they are not caused by numerical inaccuracy of the scattering wave function. It should be noted that the $1s$ TP plot has an inset at 200–250 a.u., which is plotted with a finer R spacing, thus showing the true oscillatory behavior.

The oscillations are consistent with a term of the form ne^{2ik_nR}/R, which asymptotically approaches zero, but contributes to the cross sections at finite R. The dashed lines in Fig. 1 have been scaled by $[1+n\sin(2k_nR)/R]$ to remove this term, and it is clear that these scaled results are very significantly smoother, with the exception of the $5s$ CL results.

It can also be seen from these plots that taking an average through the oscillations will also allow convergence of the cross sections to be obtained at much smaller R. The discrete cross section results presented in Tables I and II are calculated at $R=400$ a.u. and taking an average of the last oscillation.

The estimated accuracy of the TP cross sections range from 0.5% for the higher energy ($E_0>0.5$ a.u.) $1s$ results to 2.0% for the $5s$ results and lower energy ($E_0\leqslant 0.2$ a.u.) $1s$ results. The estimated error of the TICS results is 0.2%. The TP results at 1, 1.5, and 2 a.u. match the very accurate finite-difference method (FDM) results of Jones and Stelbovics [7] to within ±1 least significant digit, and the low-energy results match the results of Bray and Stelbovics [31] (interpolated with cubic splines to match data points) to within our estimated accuracy. We know of no other publications containing discrete final-state cross sections for the CL model, and estimate our errors to be the same as our TP results.

The CL model 0.1 a.u. triplet elastic cross section in Table I is highly suppressed, and from the singlet and triplet CL model cross sections in Fig. 2, it is evident that this is the result of a resonance. The singlet resonance is centered at approximately 0.051 a.u. and the triplet resonance is centered at 0.097 a.u., both of which are unphysical, and highlight the inaccuracy of the CL model at energies below ionization threshold.

TABLE II. TP model singlet and triplet electron-impact discrete final-state scattering cross sections and total ionization cross sections; see Table I for units and column details.

E_0	σ^0_{1s}	σ^0_{2s}	σ^0_{3s}	σ^0_{4s}	σ^0_{5s}	σ^0_i	σ^0_t	σ^1_{1s}	σ^1_{2s}	σ^1_{3s}	σ^1_{4s}	σ^1_{5s}	σ^1_i	σ^1_t
0.1	4.22[+0]						4.22[+0]	1.02[+1]						1.02[+1]
0.2	1.46[+0]						1.46[+0]	6.94[+0]						6.94[+0]
0.3	7.57[−1]						7.57[−1]	4.97[+0]						4.97[+0]
0.4	4.76[−1]	3.26[−2]					5.07[−1]	3.74[+0]	3.26[−4]					3.74[+0]
0.5	3.30[−1]	4.07[−2]	6.99[−3]	1.80[−3]	5.86[−4]		3.80[−1]	2.90[+0]	1.89[−3]	3.54[−5]	1.81[−6]	1.61[−7]		2.90[+0]
0.6	2.50[−1]	3.54[−2]	8.17[−3]	3.00[−3]	1.42[−3]	4.99[−3]	3.03[−1]	2.32[+0]	3.46[−3]	2.28[−4]	4.44[−5]	1.47[−5]	9.01[−6]	2.32[+0]
0.7	2.01[−1]	2.94[−2]	7.42[−3]	2.91[−3]	1.43[−3]	1.19[−2]	2.54[−1]	1.90[+0]	4.59[−3]	4.70[−4]	1.23[−4]	4.92[−5]	1.02[−4]	1.91[+0]
0.8	1.70[−1]	2.43[−2]	6.36[−3]	2.55[−3]	1.27[−3]	1.69[−2]	2.21[−1]	1.59[+0]	5.28[−3]	6.77[−4]	2.01[−4]	8.65[−5]	3.20[−4]	1.60[+0]
0.9	1.48[−1]	2.01[−2]	5.34[−3]	2.16[−3]	1.08[−3]	1.99[−2]	1.97[−1]	1.35[+0]	5.63[−3]	8.25[−4]	2.63[−4]	1.17[−4]	6.30[−4]	1.36[+0]
1.0	1.31[−1]	1.68[−2]	4.50[−3]	1.83[−3]	9.20[−4]	2.14[−2]	1.76[−1]	1.16[+0]	5.77[−3]	9.24[−4]	3.08[−4]	1.40[−4]	9.84[−4]	1.17[+0]
1.5	8.65[−2]	8.02[−3]	2.13[−3]	8.67[−4]	4.37[−4]	1.94[−2]	1.17[−1]	6.32[−1]	5.08[−3]	9.89[−4]	3.59[−4]	1.72[−4]	2.48[−3]	6.41[−1]
2.0	6.47[−2]	4.61[−3]	1.20[−3]	4.87[−4]	2.45[−4]	1.47[−2]	8.59[−2]	4.04[−1]	4.02[−3]	8.38[−4]	3.13[−4]	1.52[−4]	3.10[−3]	4.12[−1]

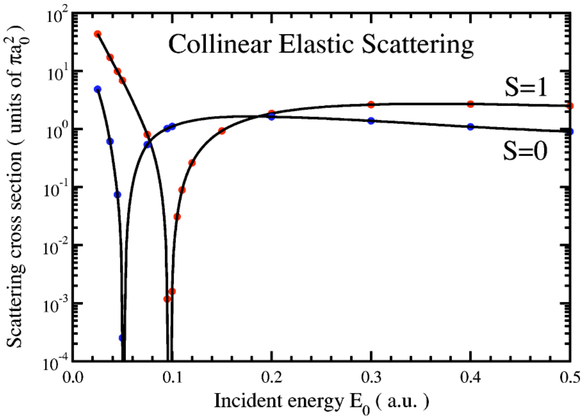

FIG. 2. CL singlet and triplet elastic scattering cross section, with spin weighting, as a function of incident-electron energy.

Examination of the cross section data in Tables I and II reveals the distinctly different behavior of the CL and TP models. The singlet elastic cross sections of the CL model are three times larger than the TP model above ionization threshold, whereas the triplet elastic cross sections are of similar magnitude. Below threshold, comparison of the elastic cross sections is difficult due to the wide resonance in the CL model. The peak singlet inelastic cross sections for each model are of similar magnitude, but are consistently shifted nearer to threshold in the CL model. The peak singlet ionization cross section of the CL model is half that of the TP model, and is once again closer to threshold.

The peak triplet inelastic and ionization cross sections of each model have similar magnitude, and are also shifted nearer threshold in the CL model, but to a lesser extent than the singlet case. For energies below the peak cross sections, the CL model cross sections are less suppressed.

B. Threshold laws and ionization cross sections

Previously [21], we presented details of our near-threshold results for the $L=0$ CL model for electron-impact with atomic hydrogen. We found the threshold behavior to be consistent with the Wannier [20] threshold law, to very high accuracy, and was able to derive a fitting function that accurately predicts the $L=0$ singlet CL TICS (in units of a_0^2) for total energies in the range 0.005–0.2 a.u.,

$$\sigma_{S=0}^{CL}=E^{(1.128\pm0.004)}((0.386\pm0.007)-E(1.69\pm0.08)+E^2(4.1\pm0.5)-E^3(4.6\pm1.1)). \tag{35}$$

Our results also gave support to the semiclassical calculations of Peterkop [22] for the CL model's triplet threshold behavior giving $E^{3.37\pm0.02}$.

Using semiclassical methods, the threshold power law for the triplet wave function for three-body breakup was first proposed by Klar and Schlecht [32] to be $E^{3.881}$. This incorrect result was repeated in subsequent publications [33,34], but was correctly calculated by Peterkop [22] to be $E^{3.381}$. This matched subsequent derivations [35,36], also using semiclassical methods. It should be noted that the threshold laws for the singlet and triplet $L=0$ partial waves of the full hydrogen problem are predicted to be the same as the $L=0$ CL model [22,27,36]. Also, the threshold law for the $L>0$ singlet and triplet partial waves for the full hydrogen problem is the same as the $L=0$ *singlet* partial wave [32–34,37].

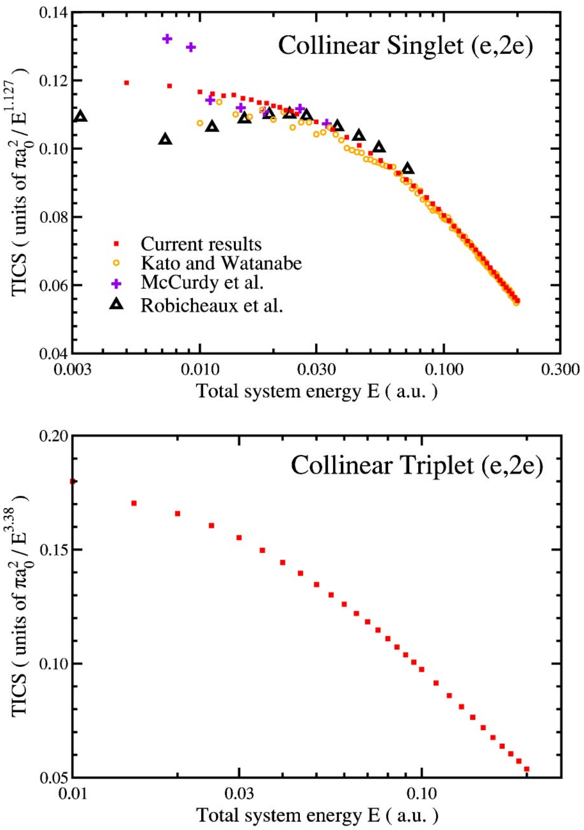

FIG. 3. CL singlet and triplet $(e,\ 2e)$ TICS, with spin weighting, as a function of total system energy near ionization threshold. The results are compared with those of Kato and Watanabe [18], McCurdy *et al.* [11], and Robicheaux *et al.* [19]. The singlet and triplet results are divided by $E^{1.127}$ and $E^{3.28}$, respectively, to emphasize their threshold behavior.

So as to provide a complete review of the threshold behavior of both models, we repeat our singlet results from our previous publication in Fig. 3, and discuss our fitting of these results in more detail.

Clearly, Fig. 3 shows good agreement between our CL model singlet TICS results and those of Kato and Watanabe [18] for all energies considered, and our results exhibit a significant reduction in the energy-dependent oscillations. However, it should be noted that the Kato and Watanabe results on our plot were obtained by scanning and digitizing their published results, and may have additional errors introduced by this process. We have good agreement with the results of McCurdy *et al.* [11] for energies above 0.01 a.u., and with Robicheaux *et al.* [19] above 0.03 a.u., but both of these data sets show significant errors below these energies. The y axis in the singlet plot has been divided by $E^{1.127}$ to highlight the threshold behavior, where it is expected that the gradient of the plots should approach zero as the energy approaches threshold, if the Wannier threshold law holds for the CL model. This is indeed the case for our results and those of Kato and Watanabe.

TABLE III. Coefficients for singlet CL model TICS nonlinear fitting for E=0.005–0.2 a.u. Figures in brackets are the standard error of the last significant figure.

n	χ^2	E^{α}	a_0	a_1E	a_2E^2	a_3E^3	a_4E^4
0	164.5	0.894(6)	0.142(2)				
1	117.0	1.071(2)	0.300(3)	−0.76(1)			
2	50.7	1.112(2)	0.359(3)	−1.35(2)	2.01(6)		
3	46.5	1.128(4)	0.386(7)	−1.69(8)	4.1(5)	−4.6(11)	
4	46.3	1.148(5)	0.43(1)	−2.4(2)	12(2)	−43(9)	75(16)

We used a nonlinear fitting procedure, similar to that described by Kato and Watanabe, over the energy range 0.005–0.2 a.u., by fitting to the function $\sigma=E^{\alpha}g(E)$, where an nth order series expansion of $g(E)$ was made.

With our fitting procedure, both the value of α and its estimated error are dependent upon the number of terms in $g(E)$ and the estimated error of each of our data points. Our initial nonlinear fit was based upon the estimated errors of our results, and the fitting function was then used to calculate the standard deviation of our results in each of four energy regions of equal size. These standard deviations were then used as an improved estimate for the absolute error of the points in that region, and a new value of α was calculated. This procedure was performed iteratively until convergence of the fitting function coefficients was obtained.

The results of our $n=0$ to $n=4$ nonlinear fits are detailed in Table III. The $n=3$ polynomial for $g(E)$ was selected as the best fit, and is used for our estimate of the threshold behavior given above. From the table we can see that the χ^2 parameter reduces with increasing *n*, indicating an increasingly better fit. The difference between the χ^2 of the $n=3$ and $n=4$ fits is not significant, indicating that over this energy range $g(E)$ can be suitably represented by a third-order polynomial. As our calculations have numerical errors, increasing the degrees of freedom of the fitting function beyond the $n=3$ case did not improve the χ^2 result and necessarily increased the standard error of the coefficients. In order to select the best fit of our results we have consistently chosen n such that χ^2 *approaches* its minimum while the maximum standard error of the coefficients remains below 25%, and the polynomial coefficients do not increase exponentially.

We also performed a nonlinear fitting of the singlet data over the smaller energy range 0.005–0.05 a.u., and present these results in Table IV. As this region is closer to threshold, it was anticipated that $g(E)$ would be suitably represented by a lower-order polynomial. However, due to the fewer number of points, and the increased estimated error of the points in this region, there is some uncertainty as to whether $n=1$ or $n=2$ provides the best fit in this region. However, the coefficients of the $n=1$ fit are consistent with the $n=3$ fit from Table III. As a test of the fitting function [Eq. (35)] we performed a linear fit of the transformed data, over the same energy intervals, and obtained the same values of α, within their estimated standard error.

TABLE IV. Coefficients for singlet CL model TICS nonlinear fitting for E=0.005–0.05 a.u.

n	χ^2	E^{α}	a_0	a_1E	a_2E^2	a_3E^3
0	55.5	1.073(2)	0.287(3)			
1	19.7	1.129(2)	0.386(3)	−1.48(3)		
2	16.7	1.152(8)	0.43(2)	−2.3(3)	7(3)	
3	17.9	1.14(2)	0.40(4)	−1.9(9)	8(16)	−56(125)

Similar procedures were applied for the CL triplet TICS presented in Fig. 3, over the energy range 0.01–0.2 a.u., which gave a fitting function (in units of a_0^2) of

$$\sigma^{CL}_{S=1}=E^{(3.365\pm0.009)}((0.56\pm0.02)-E(3.59\pm0.25)+E^2(11\pm1)-E^3(14\pm3)). \tag{36}$$

However, when applied to smaller energy ranges, or compared with the results of a linear fit of the transformed data, α did not coincide within the stated error, and the polynomial coefficients changed significantly (as they are very sensitive to small changes in α). We have therefore increased our estimated standard error, and give the $L=0$ CL triplet threshold power law as $E^{3.37\pm0.02}$. This is consistent with the semiclassical theoretical calculations of Peterkop [22], who calculated the triplet power-law coefficient to be three times larger than the singlet coefficient, that is, $E^{3.38}$. The estimated error for α is larger than our singlet result due to using fewer points, limiting R_0 to 400 a.u., and the highly suppressed triplet cross sections, all of which resulted in an increase in the estimated error or our plot points.

We now turn to the TP model for which an interesting observation was made in the classical regime [40]. It was shown that, classically, ionization cannot occur below energies of 1/6 a.u. even though it is energetically allowed. Quantum mechanically we would expect a tunneling type of suppression. For the singlet TP model Macek and Ihra [23] made a fully quantal prediction for the threshold power law of

$$\sigma^{TP}_{S=0}\propto\exp(-6.870E^{-1/6}+3.680E^{1/6}). \tag{37}$$

Later, Miyashita *et al.* performed a fit of their results (ignoring the $E^{1/6}$ term) and obtained (in units of πa_0^2)

$$\sigma^{TP}_{S=0}=(104\pm1)\exp(-(6.75\pm0.02)E^{-1/6}) \tag{38}$$

for energies approaching threshold. They also suggested replacing $E^{-1/6}$ with $E^{-\alpha}$ and calculating α from their numerical fit. There is justification for this as the derivation of $E^{-1/6}$ relied on some theoretical approximations [23]. This gave a threshold behavior of

$$\sigma^{TP}_{S=0}\propto\exp(-(8.4\pm0.1)E^{-0.149\pm0.008}). \tag{39}$$

Our TP singlet TICS results are plotted in Fig. 4. We have divided our results by fitting functions given by Miyashita *et al.* to view the energy dependence of these functions, as applied to our results. As in Fig. 3 for the CL model, we

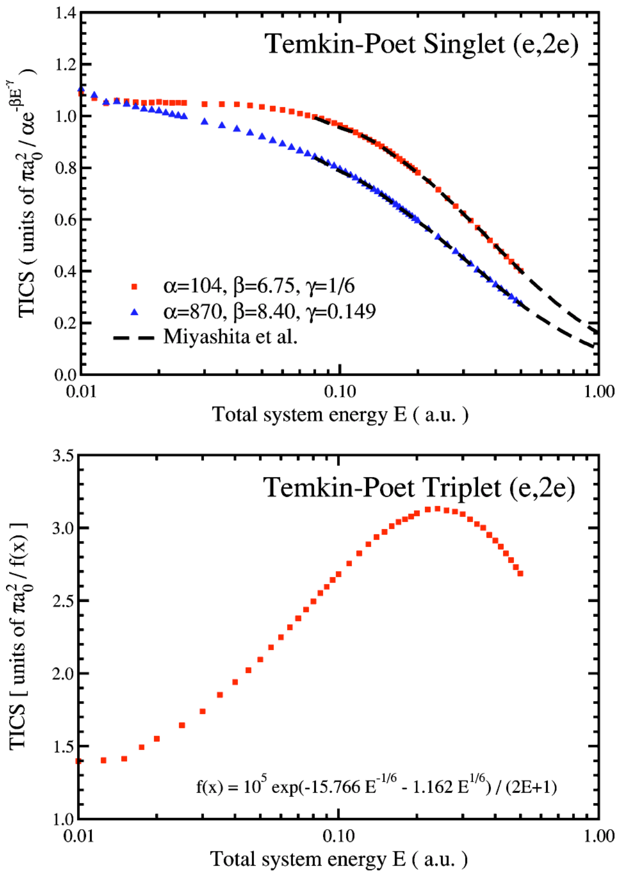

FIG. 4. TP singlet and triplet (e,2e) TICS, with spin weighting, as a function of total system energy near ionization threshold. To emphasize their threshold behavior, the singlet results are divided by the two fitting functions (see text) calculated by Miyashita *et al.* [38], and the triplet results are divided by the fitting function calculated by Ihra *et al.* [39]. The results of Miyashita *et al.* [38] for TP singlet energies 0.08–1.00 a.u. are displayed with long dashes, and are mostly indistinguishable from our results. Their results at lower energies are not displayed due to the significant errors in digitizing their published figures.

would expect the gradient of our plots to approach zero as we approach threshold, if they support the threshold law.

Using nonlinear fitting procedures we were able to fit our data to the function $\exp(aE^{-1/6})(b+cE)$ over the energy range 0.005–0.100 a.u., and obtained (in units of πa_0^2)

$$\sigma^{TP}_{S=0}=\exp(-(6.868\pm0.007)E^{-1/6}) \times\{(142\pm2)-(224\pm8)E\}, \qquad (40)$$

which matches Macek and Ihra, within estimated error.

Our fitting to the function $\exp(aE^{-b})(c+dE)$ over the same energy range gave (in units of πa_0^2)

$$\sigma^{TP}_{S=0}=\exp(-(6.7\pm0.3)E^{-0.169\pm0.004}) \times\{(117\pm39)-(181\pm73)E\}. \qquad (41)$$

The significant errors of this fit limit the conclusions that we can draw from our results. Many more data points would be required to accurately fit our data to this function, however, the $E^{-0.169\pm0.004}$ term is again consistent with the Macek and Ihra prediction of an $E^{-1/6}$ dependence.

In Fig. 4 we also present our triplet TICS results, divided by the threshold form calculated by Ihra *et al.* [39]

$$\sigma^{TP}_{S=1}\propto\frac{1}{2E+1}\exp(-15.766E^{-1/6}-1.162E^{1/6}). \qquad (42)$$

Once again, the gradient of the plot approaches zero as E approaches zero, giving support to their estimated threshold behavior for the TP triplet model. When a nonlinear fit of our results was made to this functional form, the calculated error of all the coefficients were too large to allow any conclusions to be made. This was due to the very highly suppressed cross section near threshold and the limited number of data points.

It should be noted that our fitting functions for the Temkin-Poet model [Eqs. (40) and (41)] were very sensitive to the energy range chosen for the fit, and the number of terms in the modifying polynomial. Though our results match the $E^{-1/6}$ functional form within our estimated error, giving support to its validity, the possibility of alternate forms for the threshold law that closely match our results in the energy range considered, cannot be discounted. Our tabulated results can be supplied, upon request, to interested readers for such tests.

Plots of the singlet and triplet SDCS for the CL model at several energies (consistent with Table I) are presented in Fig. 5. The singlet plots have been normalized at equal energy sharing to highlight the change in shape as a function of incident-electron energy. At 0.6 a.u. incident-electron energy the SDCS shows a slight 4% reduction at $\epsilon_1=0$, compared with $\epsilon_1=\epsilon_2$, and becomes flat near the incident energy of 0.7 a.u. Beyond this energy, there is a marked relative increase in the unequal energy-sharing region. There are no fully quantal CL model SDCS results available for comparison, however, the trend of the SDCS shape, changing from concave to convex as energy approaches threshold, is supported by the semiclassical calculations of Rost [41].

Plots of the singlet and triplet SDCS for the TP model at several energies are presented in Fig. 6. These are compared with the FDM results of Jones and Stelbovics [7], where available, and agree within 0.5%, except near equal energy sharing.

C. Final-state asymptotic continuum waves

Figure 7 shows the SDCS for the TP model using several choices for the final-state continuum waves [Φ in Eq. (25)]. Clearly the choice of two Coulomb waves [Eq. (26)] (CC) provides a very smooth SDCS, and with sufficiently large R provides results very close to the FDM results of Jones and Stelbovics [7] [see Fig. 10 for $r_1\approx r_2$ behavior]. This method was first used by McCurdy *et al.* [11], and is able to accurately calculate the magnitude of the ionization amplitude for both models considered in this paper, as well as the full hydrogen problem [12]. Unless, otherwise stated, this method has been used to calculate all TICS and SDCS calculations in this paper.

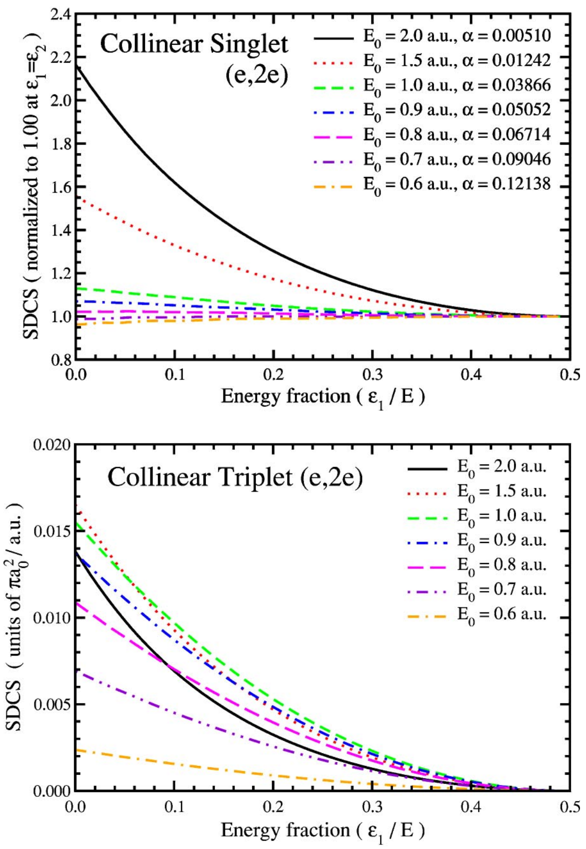

FIG. 5. CL singlet and triplet $(e,2e)$ SDCS, with spin weighting, at various incident-electron energies. The singlet plots have been normalized to 1.00 at equal energy sharing $(\epsilon_1=\epsilon_2)$, and the original SDCS may be obtained by multiplying by α $(\pi a_0^2/\text{ a.u.})$.

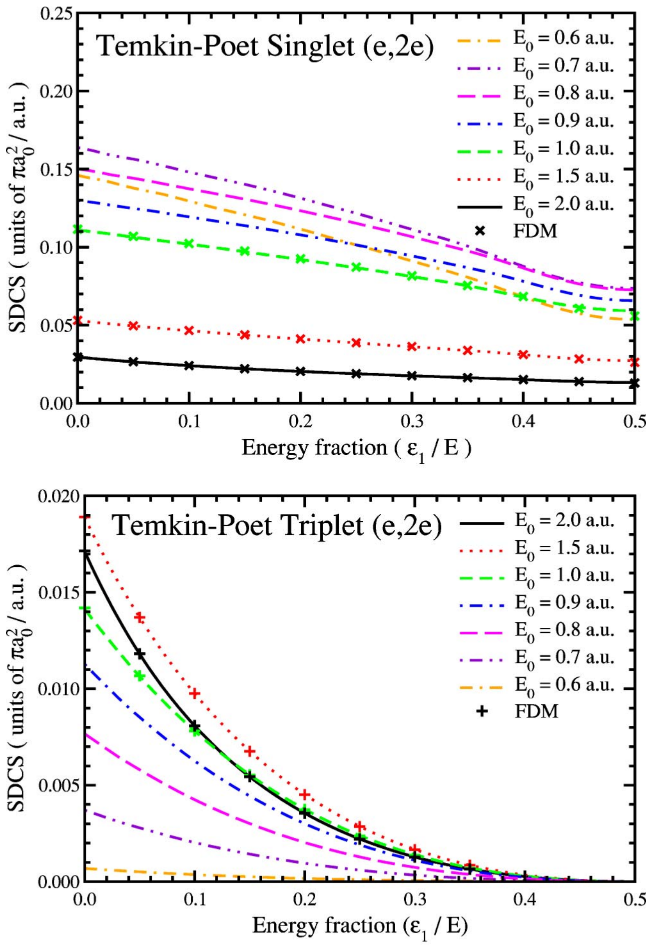

FIG. 6. TP singlet and triplet SDCS, with spin weighting, at various incident-electron energies. FDM results are by Jones and Stelbovics [7].

However, it is known that in the TP model the asymptotic form of the final-state continuum waves is approximated by a Coulomb wave for the slow electron and a plane wave for the fast electron. When Eq. (27) was used with our scattering wave function, however, the SDCS oscillated wildly, due to interference with discrete final-state scattering also contained in the scattering wave function. Figure 7 shows that the SDCS results using a Coulomb wave and an orthogonalized plane wave (CO) [see Eq. (28)] removes this problem, and gives results very similar to the (CC) results, but with minor fluctuations of the order of 1%. These fluctuations diminish with increasing R. For the case of two orthogonalized plane waves (OO), good results are obtained near equal energy sharing, but significant oscillations are apparent at asymmetric energy sharing.

In Fig. 8 we have plotted the phase of the ionization amplitude [Eq. (25)] extracted at various R. The Coulomb phase(s) has been excluded from all phase plots in this paper as it is known to be highly oscillatory when k approaches zero. For the TP model, it is apparent that the phase is divergent when CC are used for the final-state continuum waves, and is consistent with the known logarithmic phase behavior of this final state. However, the phase is convergent when CO are used for the final-state continuum waves. The slight increase in phase shown on the $R=1000$ a.u. CO plot does not indicate a slowly diverging phase. Our convergence studies showed that our primary grid spacing (0.40 a.u. at this energy) was required to be halved in order to provide stable phase results with increasing R, indicating that convergence of the phase results is much more sensitive to the numerical

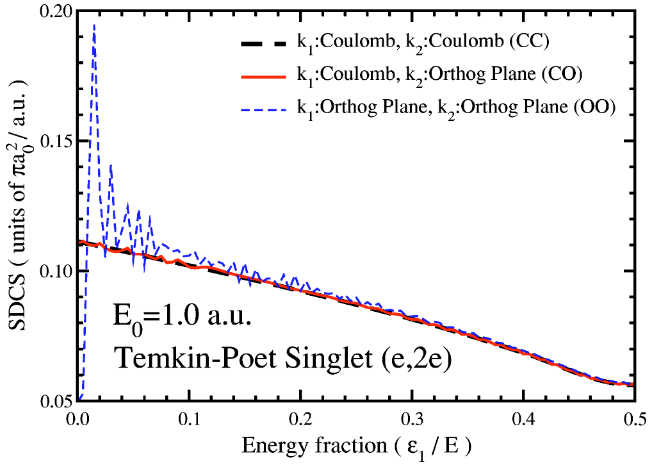

FIG. 7. TP singlet SDCS, with spin weighting, at 1.0 a.u. incident-electron energy (27.2 eV) for various choices for the final-state continuum waves, extracted at $R=1000$ a.u.

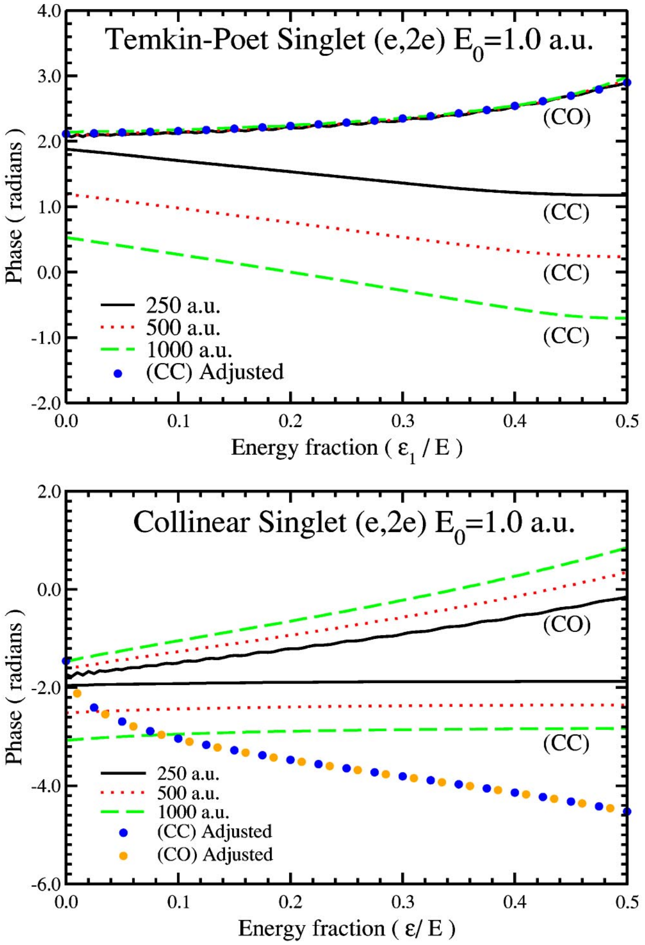

FIG. 8. TP and CL singlet ionization amplitude phase using the final-state continuum wave approximation of two Coulomb waves (CC), and an orthogonalized plane wave for the fast electron and a Coulomb wave (CO) for the slow electron, extracted using the surface integral Eq. (25) at the hyperradii $R = 250$, 500, and 1000 a.u. Adjusted results have been made by adding phase adjustments [Eq. (43)–(45)] to our raw results.

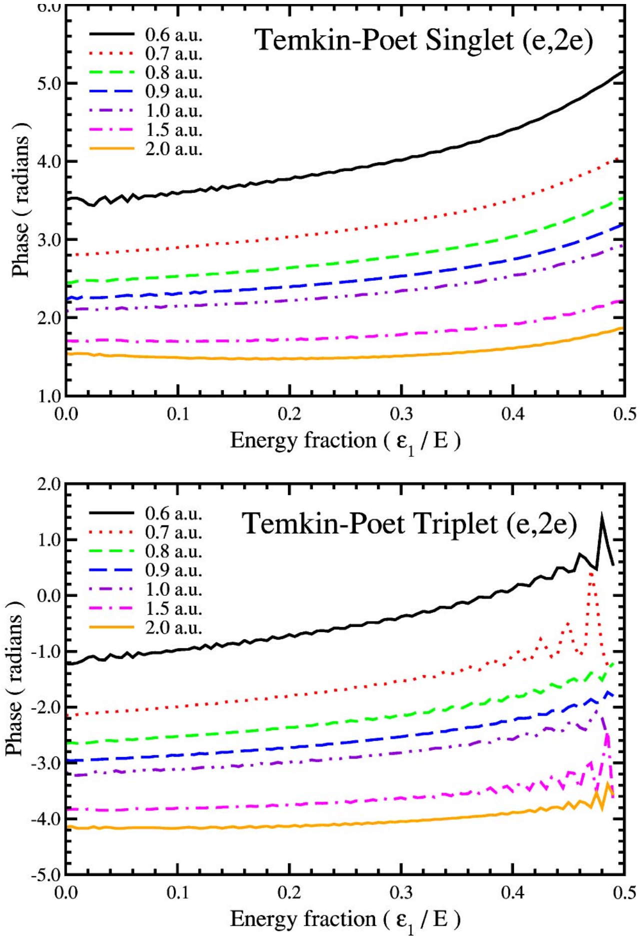

FIG. 9. TP singlet and triplet ionization amplitude phases at various incident-electron energies, using a Coulomb wave for the slow electron and an orthogonalized Coulomb wave for the fast electron.

errors introduced by finite grid methods.

For the CL model, however, neither the CC nor CO final-state continuum waves provide convergent phase results, as neither describes the true asymptotic form of the continuum waves in this model.

Recently Rescigno *et al.* [25] were able to demonstrate that the ionization amplitude phase for both the CL and TP models could be made convergent, and for the TP model match the (CO) results presented in Fig. 8. Their procedure can be applied to any choice of charges for the final-state Coulomb waves, by adding the logarithmic phase factors, including the Peterkop phase. Their phase adjustment equations for the two models are

$$\phi_{\mathrm{TP}} = \left(\frac{1}{k_<} - \frac{z_1}{k_1} - \frac{z_2}{k_2} \right) \ln(2KR), \qquad (43)$$

$$\phi_{\mathrm{CL}} = \left(\frac{1-z_1}{k_1} + \frac{1-z_2}{k_2} - \frac{1}{k_1+k_2} \right) \ln(2KR), \qquad (44)$$

and

$$Q(k;z) = \arg\left(\Gamma\left(1 - i\frac{z}{k} \right) + 2\frac{z}{k} \ln(k/K) \right). \qquad (45)$$

The phase adjustment for the TP model is therefore zero for the CO case, and $\phi_{TP} + Q(k_>,1)$ for the CC case. The phase adjustment for the CL model is ϕ_{CL} for the CO case and $\phi_{CL} + Q(k_>,1)$ for the CC case.

These phase adjustments have been applied separately to our CL and TP model results in Fig. 8, and demonstrate that the adjustments give R-convergent phases that are independent of the z_1 and z_2 choice for the final-state asymptotic continuum waves.

Figure 9 shows the ionization amplitude phase for the TP model singlet and triplet states at various incident-electron energies, using the CO final-state asymptotic continuum waves. The phase is clearly energy dependent, and the plots also demonstrate a systematic flattening (with respect to the ϵ_1 energy fraction) with increasing incident-electron energy E_0. These plots were extracted at varying hyperradii (400–1000 a.u.), where good convergence of the SDCS were obtained, and demonstrate only minor fluctuations in the phase, except near equal energy sharing in the triplet plots, where the ionization amplitudes are highly suppressed.

D. Grid spacing and convergence issues

The scattering wave functions for the electron impact of hydrogen, and the simplified models presented in this paper, are highly oscillatory. The wavelength of these oscillations determines the grid spacing, and the magnitude of their high-order derivatives determines the accuracy, of the finite difference methods used for their solution. For discrete final-state scattering, the scattering amplitude information is contained mostly within the region where r_1 or r_2 are between $0-4n^2$ a.u., where n is the final-state orbital quantum number. The wavelength of the primary oscillations of the wave function in this region are determined by the momentum of the elastically scattered electron, $\lambda=2\pi/\sqrt{2E_0}$. For ionization, however, the ionization amplitude information is contained in the region where $r_1\approx r_2$, where the wavelength of the wave function is determined (asymptotically) from the total system energy $\lambda=2\pi/\sqrt{2E_0-1}$. The wavelength of the wave function is therefore at a minimum when $r_1\rightarrow 0$ or $r_2\rightarrow 0$, and this region determines the primary grid spacing of our grids. Extraction of the ionization cross sections on the hypersphere, as presented in Sec. II D, requires the wave function to be accurate over both of these regions and so our grid spacing convergence studies have been performed using the SDCS calculated with Eq. (25).

Near the nucleus, the high electrostatic potentials cause distortions to the wave function, increasing the high-order derivatives in this region, and thus requiring finer grid spacing to maintain accuracy of the Numerov method.

A detailed convergence study of the SDCS extracted from the CL and TP wave functions was undertaken at several energies so that we could verify the energy dependence of the grid spacing and calculate the grid size required to provide accurate results for each of these models. We did not observe any significantly different behavior between the models, apart from the very large R_0 required in the TP model to obtain convergence of the SDCS near equal energy sharing, as is evident in Fig. 10. It can be seen that good convergence of the SDCS is obtained for the TP model at 1.0 a.u. and $R=400$ a.u., except near equal energy sharing. The nonanalytic nature of the potential $(1/r_>)$ at $r_1=r_2$ is believed to be the reason for the slow convergence of the SDCS in this region. However, it should be noted that the lack of convergence in the SDCS in this region has negligible effect upon the TICS calculated from these plots, and that the TICS can be calculated very accurately when $R_0\approx 400$ a.u., at this energy. The problem of slow convergence of the SDCS at equal energy sharing in the TP model was also observed by Jones and Stelbovics [7].

For the CL model with an incident-electron energy of 0.7 a.u., the grid spacing in Table V was used to obtain convergence of the TICS to better than 0.2%, and convergence of the SDCS at all energy fractions to better than 0.5%.

As seven regions of grid spacing were used in our calculations, with three other grid parameters, R_0, R_{max}, and θ, it may be possible to obtain results of similar accuracy with a more relaxed grid spacing in some regions, but the very large number of possible grid spacing combinations, meant that only a limited number of these possibilities could be tested. However, several interesting observations were noted during our convergence testing.

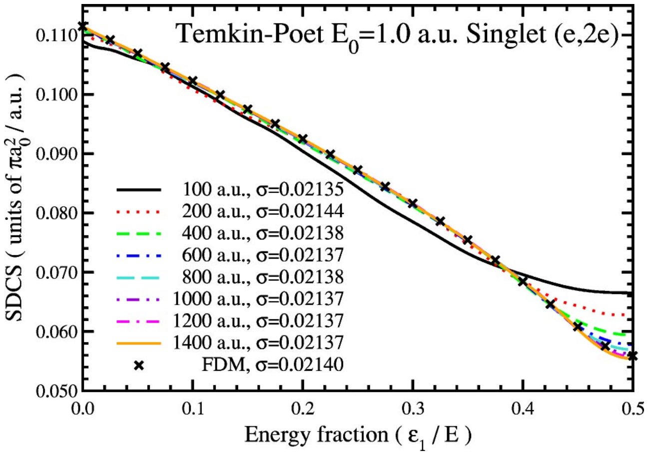

FIG. 10. TP singlet SDCS, with spin weighting, at an incident-electron energy of 1.0 a.u. (27.2 eV), extracted using two Coulomb waves for the final-state continuum waves, at various hyperradii R. FDM results are by Jones and Stelbovics [7]. The TICS calculated at each R are displayed in the legend (units of πa_0^2).

First, the shape of the SDCS only varied with the selection of R_0, other grid spacing (within limits) only served to offset the SDCS from the converged position. Therefore, if less accuracy is acceptable, the grid spacing can be relaxed, and the cross sections can be extracted from wave functions calculated with significantly fewer grid points, which would require significantly less computing resources.

Second, a significant reduction in the R_0 dependence of the TICS was made by using a finer grid spacing about R_0, where complex scaling begins. We believe this to be due to the discontinuous first derivative of the complex scaled wave function at these points. As the complex-scaling begins at different relative phases of the wave function with different R_0, the finer grid spacing reduces the error in the finite-difference method at this discontinuity.

Third, a very fine grid ($h_1=0.01$ a.u.) was required near the origin due to the large Coulomb interactions in this region, and is possibly also due to the polynomial approxima-

TABLE V. Grid spacing used at 0.7 a.u. incident-electron energy, with $R_0=600$ a.u., $\theta=0.8$ rad, with all spacing measured along the real axis.

Region (n)	Start (a.u.)	Length (a.u.)	Spacing h_n (a.u.)
1	0.0	1.0	0.01
2	1.0	10.0	0.10
3	11.0	20.0	0.20
4	31.0	30.0	0.30
5	61.0	537.0	0.50
6	598.0	4.0	0.10
7	602.0	13.0	0.50

tion of ψ used to derive the Numerov formula at the singularities (when $r_1=0$ or $r_2=0$). Though, the spacing can be increased to 0.05 a.u. without introducing large inaccuracies. Also, it should be noted that complete convergence was not obtained with the main grid spacing of $h_5=0.50$ a.u., but was selected to balance computational effort with desired accuracy. Complete convergence is obtained with $h_5=0.30$ a.u.

Also, to ensure that setting $\psi(R_{max},r_2)=0$ and $\psi(r_1,R_{max})=0$ is an accurate approximation and does not affect the accuracy of the wave function on the real grid, $R_{max}-R_0$ (the complex-scaled region of the grid) must be sufficiently large such that it contains approximately 1.5, or more, oscillations of the wave function in its least oscillatory region (along $r_1=r_2$). Therefore, the length of the complex-scaling region is energy dependent.

Lastly, the following approximate energy relationships were used to calculate the grid spacing for our models at other energies, using the 0.7 a.u. convergence testing to calculate the proportionality constants:

$$h_n \propto 1/\sqrt{(2E_0)}, \tag{46}$$

where E_0 is the energy of the incident electron (in a.u.), indicating that the grid spacing is governed by the $r_1 \ll R_0$ or $r_2 \ll R_0$ regions of the wave function, which contain the discrete final-state scattering information. For ground-state scattering

$$R_{max}-R_0 \propto 1/\sqrt{(2E_0-1)}, \tag{47}$$

indicating that the length of the complex-scaling region is determined by the number of oscillations in the least oscillatory region of the wave function, where $r_1=r_2$.

For our calculations we obtained convergent results when $R_0 \approx 40(R_{max}-R_0)$. However, for total system energies below 0.04 a.u., this results in an R_0 greater than the largest value that we used in our calculations (1400 a.u.), so the estimated error of our TICS for these low energies was increased to 0.5–1.0 %. There was little variation in our results for different complex-scaling angles θ, and 0.8 radians was used for all the results presented in this paper.

We used the same grid spacing for discrete final-state scattering and checked that this also provided convergent results. However, for energies below ionization threshold, the wave function is (for large R) highly suppressed in the region $r_1 \approx r_2$, and the complex scaling region $(R_{max}-R_0)$ was limited to 50 a.u.

V. CONCLUSION

For the $L=0$ CL and TP models, the scattering wave function calculated using ECS and our propagation method can be used to extract both ionization and discrete final-state scattering cross sections to high accuracy. Also, with the correct choice of final-state asymptotic continuum waves, convergent ionization amplitude phases can be obtained directly for the TP model. Moreover, as discovered by Rescigno *et al.* [25], converged ionization amplitudes can be extracted for any general final-state continuum wave choice for both the CL and TP models.

Due to the very efficient propagation algorithm that we have used in our ECS implementation, we have been able to extend the computation grid to very large distances (>1400 a.u.). This has allowed us to accurately calculate TICS results for very low impact energies (<0.505 a.u., 13.75 eV), which has in turn allowed us to investigate the threshold behavior for the singlet and triplet wave functions for the CL and TP models to high accuracy. The threshold behavior is highly model dependent, and our results support the classical calculations of Wannier [20] for the $L=0$ CL singlet model, the semiclassical calculations of Peterkop [22] for the $L=0$ CL triplet model, and is consistent with the fully quantal prediction of Macek and Ihra [23] for the TP singlet model, and the fully quantal prediction of Ihra *et al.* [39] for the TP triplet model.

These model problems have successfully tested the use of the propagation method with ECS, and paved the way for efficiently calculating solutions to the numerically intensive full hydrogen problem. Further, with the efficiency gains achieved by the propagation method, a fully quantal solution of the Coulomb four-body problem is, in the not to distant future, a distinct possibility.

ACKNOWLEDGMENTS

The authors would like to thank Igor Bray for his efforts in obtaining the computing resources required to support this project, and acknowledge the support of the Australian Research Council (ARC), the Australian Partnership for Advanced Computing (APAC), and the Western Australian Interactive Virtual Environments Center (IVEC).

APPENDIX: NUMEROV FORMULA

Four variations of the Numerov formula are required to compute the scattering wave function at different points on the grid, and their selection depends on whether $r_{i-1}=0$ and/or $r_{j-1}=0$, dictating whether a series expansion for $\psi_{i,0}$ and/or $\psi_{0,j}$ is used when deriving the formula. These Numerov formulas may be most simply represented by

$$\sum_{i'=-1}^{1}\sum_{j'=-1}^{1}\{(h^2\mathcal{B}_{i'}\mathcal{C}_{j'}+t^2\mathcal{A}_{i'}\mathcal{D}_{j'})\psi(r_{i+i'},r_{j+j'}) + h^2t^2\mathcal{B}_{i'}\mathcal{D}_{j'}\Omega(i+i',j+j')\}=0, \tag{A1}$$

where from Eqs. (3) and (6) we obtain

$$\Omega(i,j)=2\left(E+\frac{1-\delta_{i,0}}{r_i}+\frac{1-\delta_{j,0}}{r_j}-V_{12}(r_i,r_j)\right)\psi(r_i,r_j) - 2\chi(r_i,r_j), \tag{A2}$$

and where h and t are the grid spacing in the i and j directions, respectively, given by $h=r_i-r_{i-1}$ and $t=r_j-r_{j-1}$. Two further coefficients are used, $\alpha=(r_{i+1}-r_i)/h$ and $\beta=(r_{j+1}-r_j)/t$, which determine the expansion (or contraction) of the grid spacing in the i and j directions, respectively.

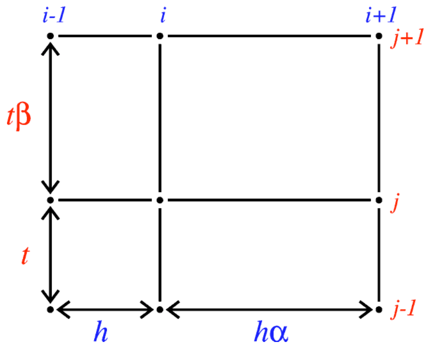

FIG. 11. The grid spacing in the i direction and j direction may be nonuniform, either real or complex, and is measured by the parameters h and t and the expansion (or contraction) ratios α and β.

Each grid measurement, h, t, α, and β may be real or complex, and are displayed graphically in Fig. 11. The values of $\mathcal{A}$, $\mathcal{B}$, $\mathcal{C}$, and $\mathcal{D}$ vary depending on whether $r_{i-1}=0$ and / or $r_{j-1}=0$.

First, we shall consider only the i direction. If there is no singularity $r_{i-1}>0$ then

$$\mathcal{A}_{-1}=12\alpha,$$

$$\mathcal{A}_0=-12(\alpha+1),$$

$$\mathcal{A}_1=12,$$

$$\mathcal{B}_{-1}=-\alpha^3+\alpha^2+\alpha,$$

$$\mathcal{B}_0=\alpha^3+4\alpha^2+4\alpha+1,$$

$$\mathcal{B}_1=\alpha^2+\alpha-1. \tag{A3}$$

When there is a singularity $r_{i-1}=0$ then

$$\mathcal{A}_{-1}=0,$$

$$\mathcal{A}_0=(\alpha+1)(3\lambda^2\alpha^2h^2+4\lambda^2h^2\alpha-30\lambda\alpha h+\lambda^2h^2$$
$$-24\lambda h+72),$$

$$\mathcal{A}_1=-\lambda^2h^2-6\lambda\alpha h+2\lambda^2h^2\alpha+24\lambda h-72,$$

$$\mathcal{B}_{-1}=6\alpha(\alpha^2-\alpha-1),$$

$$\mathcal{B}_0=(\alpha+1)(3\lambda\alpha^2h-6\alpha^2-18\alpha+4\lambda\alpha h+\lambda h-6),$$

$$\mathcal{B}_1=2\lambda\alpha^2h-6\alpha^2+\lambda\alpha h-\lambda h-6\alpha+6. \tag{A4}$$

The value of λ in these equations is set to $2z$ where z is the charge on the nucleus.

For the j direction, the formulas are similar to those above and are selected on whether there is a singularity, $r_{j-1}=0$, or not, $r_{j-1}>0$. We let $\mathcal{C}_{j'}=\mathcal{A}_{i'}$ and $\mathcal{D}_{j'}=\mathcal{B}_{i'}$, except that α is replaced by β, and h is replaced by t.

---

[1] M. Baertschy, T.N. Rescigno, W.A. Isaacs, X. Li, and C.W. McCurdy, Phys. Rev. A **63**, 022712 (2001).
[2] A.S. Kadyrov, A.M. Mukhamedzhanov, and A.T. Stelbovics, Phys. Rev. A **67**, 024702 (2003).
[3] R. Poet, J. Phys. B **13**, 2995 (1980).
[4] A. Temkin, Phys. Rev. **126**, 130 (1962).
[5] R. Poet, J. Phys. B **11**, 3081 (1978).
[6] S. Jones and A.T. Stelbovics, Aust. J. Phys. **52**, 621 (1999).
[7] S. Jones and A.T. Stelbovics, Phys. Rev. A **66**, 032717 (2002).
[8] M. Baertschy, T.N. Rescigno, W.A. Isaacs, and C.W. McCurdy, Phys. Rev. A **60**, R13 (1999).
[9] T.N. Rescigno, C.W. McCurdy, W.A. Isaacs, and M. Baertschy, Phys. Rev. A **60**, 3740 (1999).
[10] C.W. McCurdy and T.N. Rescigno, Phys. Rev. A **62**, 032712 (2000).
[11] C.W. McCurdy, D.A. Horner, and T.N. Rescigno, Phys. Rev. A **63**, 022711 (2001).
[12] M. Baertschy, T.N. Rescigno, and C.W. McCurdy, Phys. Rev. A **64**, 022709 (2001).
[13] R. Peterkop and L. Rabik, J. Phys. B **5**, 1823 (1972).
[14] A. Temkin and Y. Hahn, Phys. Rev. A **9**, 708 (1974); see footnote [3] of this publication regarding priority over R. Peterkop and L. Rabik, J. Phys. B **5**, 1823 (1972).
[15] T.N. Rescigno, M. Baertschy, D. Byrum, and C.W. McCurdy, Phys. Rev. A **55**, 4253 (1997).
[16] R.K. Peterkop, Opt. Spectrosc. **13**, 87 (1962).
[17] M.R.H. Rudge and M.J. Seaton, Proc. R. Soc. London, Ser. A **283**, 262 (1965).
[18] D. Kato and S. Watanabe, J. Phys. B **29**, L779 (1996).
[19] F. Robicheaux, M.S. Pindzola, and D.R. Plante, Phys. Rev. A **55**, 3573 (1997).
[20] G.H. Wannier, Phys. Rev. **90**, 817 (1953).
[21] P.L. Bartlett, A.T. Stelbovics, and I. Bray, Phys. Rev. A **68**, 030701(R) (2003).
[22] R. Peterkop, J. Phys. B **16**, L587 (1983).
[23] J.H. Macek and W. Ihra, Phys. Rev. A **55**, 2024 (1997).
[24] P.L. Bartlett, I. Bray, S. Jones, A.T. Stelbovics, A.S. Kadyrov, K. Bartschat, G.L. Ver Steeg, M.P. Scott, and P.G. Burke, Phys. Rev. A **68**, 020702(R) (2003).
[25] T.N. Rescigno, M. Baertschy, and C.W. McCurdy, Phys. Rev. A **68**, 020701(R) (2003).
[26] Nonzero angular momentum waves present no additional complications for the algorithms used.
[27] R. K. Peterkop, *Theory of Ionization of Atoms by Electron Impact* (Colorado Associated University Press, Boulder, CO, 1977).
[28] Y.D. Wang and J. Callaway, Phys. Rev. A **48**, 2058 (1993).
[29] S. Jones and A.T. Stelbovics, Phys. Rev. Lett. **84**, 1878 (2000).
[30] M. Abramowitz and I. A. Stegun, *Handbook of Mathematical Functions with Formulas, Graphs and Mathematical Tables* (Dover, New York, 1965).
[31] I. Bray and A.T. Stelbovics, At. Data Nucl. Data Tables **58**, 67 (1994).
[32] H. Klar and W. Schlecht, J. Phys. B **9**, 1699 (1976).
[33] C.H. Greene and A.R.P. Rau, Phys. Rev. Lett. **48**, 533 (1982).

[34] C.H. Greene and A.R.P. Rau, J. Phys. B **16**, 99 (1983).
[35] J.M. Feagin, J. Phys. B **17**, 2433 (1984).
[36] J.-M. Rost, J. Phys. B **28**, 3003 (1995).
[37] T.A. Roth, Phys. Rev. A **5**, 476 (1972).
[38] N. Miyashita, D. Kato, and S. Watanabe, Phys. Rev. A **59**, 4385 (1999).
[39] W. Ihra, F. Mota-Furtado, P.F. O'Mahony, and J.H. Macek, Phys. Rev. A **55**, 3250 (1997).
[40] H. Friedrich, W. Ihra, and P. Meerwald, Aust. J. Phys. **52**, 323 (1999).
[41] J.-M. Rost, Phys. Rev. Lett. **72**, 1998 (1994).